

Carbon monoxide–silicon carbide interaction in HTGR fuel particles

KAZUO MINATO, TORU OGAWA, SATORU KASHIMURA,
KOUSAKU FUKUDA, ISHIO TAKAHASHI*

*Departments of Fuels and Materials Research and *Department of Research Reactor Operation, Japan Atomic Energy Research Institute, Tokai-mura, Ibaraki-ken 319-11, Japan*

MICHIO SHIMIZU, YOSHINOBU TAYAMA

Department of JMTR Project, Japan Atomic Energy Research Institute, Oarai-machi, Ibaraki-ken 311-13, Japan

The corrosion of the coating-layers of silicon carbide (SiC) by carbon monoxide (CO) was observed in irradiated Triso-coated uranium dioxide particles, used in high-temperature gas-cooled reactors, by optical microscopy and electron probe micro-analysis. The mechanical failure of the coating-layer of inner dense pyrolytic carbon (IPyC) was often observed beside the area of the SiC corrosion. The grain boundaries of the SiC seemed to be selectively corroded during early stages of corrosion. Silicon dioxide, or more stable (Si, Ce, Ba) oxide, was accumulated at the buffer–IPyC and IPyC–SiC interfaces on the cold side of the particles and the formation of (Pd, Rh, Ru, Tc, Mo) silicides was observed in the fuel kernels, which probably resulted from the vapour transport of silicon monoxide from the corroded areas.

1. Introduction

Triso-coated fuel particles for high-temperature gas-cooled reactors consist of microspherical fuel and coating layers of porous pyrolytic carbon (PyC), inner dense PyC (IPyC), silicon carbide (SiC), and outer dense PyC (OPyC). The function of these coating-layers is to retain fission products within the particle. Because the SiC layer acts as a diffusion barrier to metallic fission products and as a pressure vessel of the particle, irradiation performance of the particles mainly depends on the integrity of the SiC layer.

In the case of the oxide fuel, carbon monoxide (CO) will be formed in the particles: the PyC layer surrounding the fuel kernel reacts with oxygen in the unirradiated fuel and with some amount of oxygen liberated from heavy metal atoms by fission, because fission products cannot bind all oxygen liberated by fission. The contribution of carbon dioxide (CO₂) is below a few per cent under typical operating conditions [1].

It has been pointed out that corrosion of the SiC layer by reaction with CO gas is a potential problem

in the oxide fuel [2–4]. The SiC layer is usually protected from CO gas by the IPyC layer, but in case of the latter's failure CO gas will come into contact with the SiC layer. Corrosion of the SiC layer was observed in thermal gradient heating of unirradiated Triso-coated (Th, U)O₂ particles without IPyC layers [2]. Out-of-reactor experiments on CO–SiC interactions have been reported [5, 6], but few reports dealt with the reaction in irradiated coated particles.

In the present work, irradiated Triso-coated low-enriched UO₂ particles were observed by optical microscopy and electron probe micro-analysis in a study of the corrosion of the SiC layers by CO gas.

2. Experimental procedure

2.1. Samples

Samples were Triso-coated low-enriched UO₂ particles irradiated in the Japan Materials Testing Reactor (JMTR). Diameter, density and ²³⁵U enrichment of the fuel kernels, and thickness and density of the coating layers are listed in Table I. The coated

TABLE I Characteristics of the samples

Particle	UO ₂ kernel			Buffer layer		IPyC layer		SiC layer		OPyC layer	
	Diam. (μm)	Density (Mg m ⁻³)	Enrich. (wt %)	Thick. ^a (μm)	Density (Mg m ⁻³)	Thick. ^a (μm)	Density (Mg m ⁻³)	Thick. ^a (μm)	Density (Mg m ⁻³)	Thick. ^a (μm)	Density (Mg m ⁻³)
77FPC1	613	10.6	4	56 ± 5	1.18	30 ± 3	1.81	29 ± 1	3.20	47 ± 4	1.84
79FPC1	623	10.5	8	63 ± 4	1.17	31 ± 3	1.87	27 ± 2	3.21	46 ± 4	1.87
80FPC1	596	10.5	8	59 ± 9	1.12	29 ± 4	1.86	24 ± 1	3.21	44 ± 6	1.83

^a Mean ± S.D.

TABLE II Irradiation conditions of samples

Sample	Capsule	Compact	Particle	Irradiation conditions				
				Time (EFPD) ^a	Temp. _(av) ^b (°C)	Temp. _(max) ^c (°C)	Burn-up (%FIMA)	Fast neutron fluence (10 ²⁵ m ⁻² , E > 29 fJ)
P-11	77F-5A	77FP2A-4 ^d	77FPC1	183.4	1065	1135	1.6	0.4
P-21, P-22	78F-3A	79FP2A-14 ^e	79FPC1	81.9	1500	1550	5.2	3.0
P-31	78F-3A	79FP2A-15 ^e	79FPC1	81.9	1340	1475	3.6	2.3
P-41	80F-6A	80FP3A-6 ^d	80FPC1	116.9	1510	1685	3.5	1.4
P-51, P-52	80F-6A	80FP3A-8 ^d	80FPC1	116.9	1500	1630	3.8	1.6
P-61	82F-1A	T82F1A-8 ^f	80FPC1	85.7	1415	1475	4.8	2.4

^a Effective full-power days.

^b Time-averaged temperature.

^c Maximum in temperature history.

^d 36 o.d. × 18 i.d. × 36 L (mm).

^e 24 o.d. × 8 i.d. × 36 L (mm).

^f 24 o.d. × 12 i.d. × 24 L (mm).

fuel particles were irradiated in the form of fuel compacts, where the coated fuel particles were dispersed in a graphite matrix. Irradiation conditions of the samples [7] are shown in Table II. Six kinds of sample with different irradiation conditions were examined, where the average temperatures ranged between 1065 and 1510 °C and the burn-up between 1.6% and 5.2% FIMA (Fissions per Initial Metal Atom).

2.2. Methods

The fuel compacts or the coated particles removed from the compacts were embedded in epoxy resin and polished with standard hot-cell ceramography technique. Polished particles were observed with the optical microscope and the shielded electron probe micro-analyser. This instrument is equipped with both wavelength-dispersive and energy-dispersive spectrometers. In order to prevent the samples from charging-up during the analysis, gold was vapour deposited on the polished surface of the samples before examination with the electron probe micro-analyser.

3. Results

3.1. Optical microscopy

On observation of the polished surface of irradiated particles by optical microscopy, some particles were found with corroded SiC layers. The observed morphology of the corroded area was different from that by palladium [8–10] and by rare-earth elements [11, 12]. Typical examples of the corrosion are shown in Fig. 1. Mechanical failure of the IPyC layer as well as corrosion of the SiC layer is seen in Fig. 1a and b. Corrosion of the SiC layers in Fig. 1b and c seems to occur along the grain boundaries of the SiC. Small, white precipitates are observed at the corroded area in Fig. 1b. The SiC layer in Fig. 1d is reacted completely throughout the thickness.

It is possible to determine the direction of the temperature gradient when the kernel migrates in the particle. The kernel migrates from the cold to the hot side of the particle during high-temperature irradiation [13]. However, no kernel migration was observed

in the particles shown in Fig. 1. Because the temperature at the inner surface of a compact is higher than that at its outer surface during irradiation, the direction of the temperature gradient in the particles dispersed in the compact could be determined provided that the axial temperature gradient of the compact is negligible. The samples of P-51 and P-41 particles were polished as for the compacts, where the corroded areas were not always on the hot side of the particles.

Characteristics of the corrosion of the SiC layer observed by optical microscopy were: (1) the mechanical failure of the IPyC layer was often observed beside the area of the SiC corrosion, (2) the corroded areas were not always on the hot side of the particles, (3) the grain boundaries of the SiC seemed to be selectively corroded during the early stages of the corrosion, and (4) the IPyC and the SiC layers were often partly detached in the particles with corroded SiC layers.

3.2. Electron probe micro-analysis

Some particles were examined with the electron probe micro-analyser after the optical microscopic observation. Secondary electron images (SEI) of coating layers in the sample P-31 particle are shown in Fig. 2. The corrosion of the SiC layer is seen in Fig. 2a and the coating layers in Fig. 2b are on the opposite side to the SiC corrosion. The SiC and IPyC layers in Fig. 2b are debonded from each other and white products are seen between the layers. Energy dispersive analysis revealed that the white products contained silicon, cerium and barium.

Similar products are seen in the gap between the SiC and IPyC layers on the cold side of the sample P-52 particle in Fig. 3. The SiC layer was corroded by CO at the hot side of the particle. The corrosion of the SiC layer by palladium is also seen in Fig. 3. X-ray images in Fig. 3 indicate that the white products in the gap between the SiC and IPyC layers are (Si, Ba, Ce) oxide.

Fig. 4 shows the hot side of the coating layers with the SiC layer corroded in the sample P-22 particle, where the fuel kernel somewhat migrated. It is seen in Fig. 4 that silicon is transferred from, and that carbon

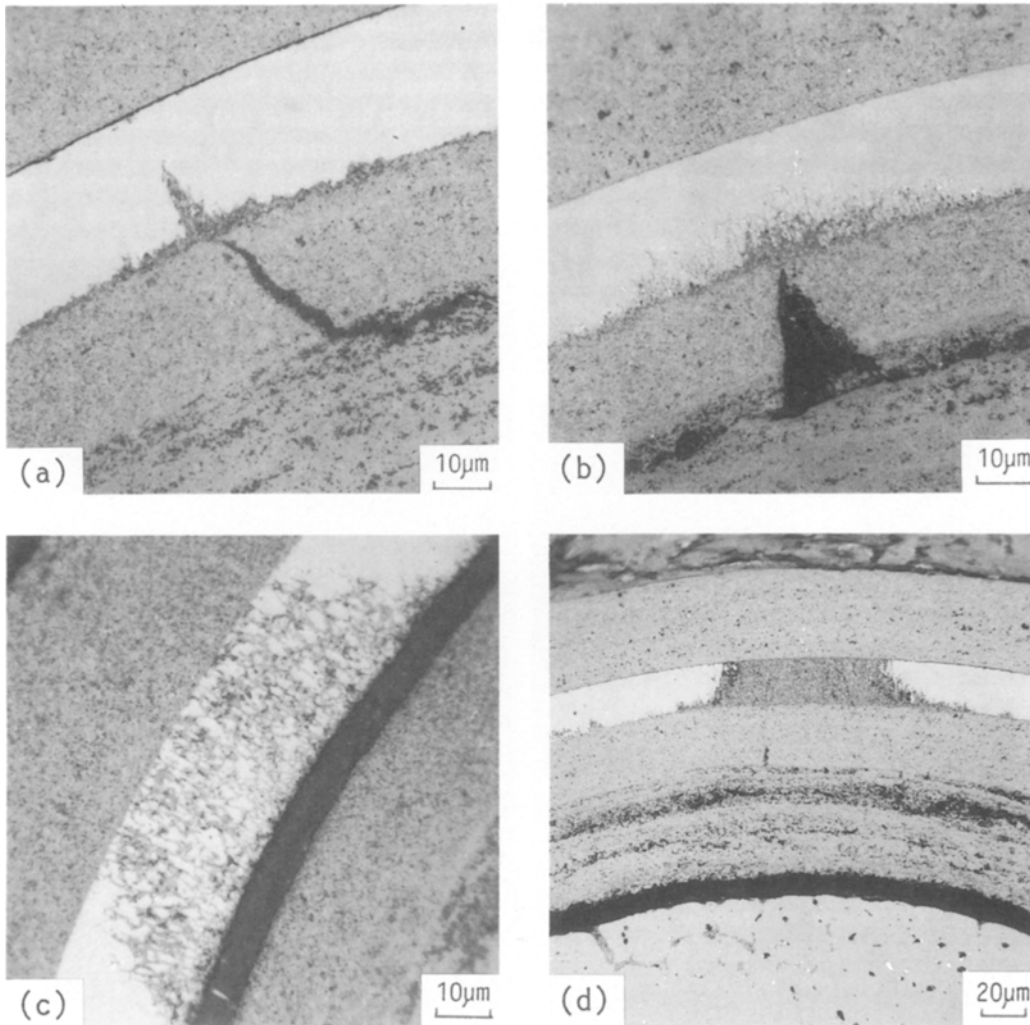


Figure 1 Corrosion of the SiC layers by CO in irradiated Triso-coated UO₂ particles observed by optical microscopy. (a) Sample P-11 particle, (b) sample P-51 particle, (c) sample P-21 particle, (d) sample P-41 particle.

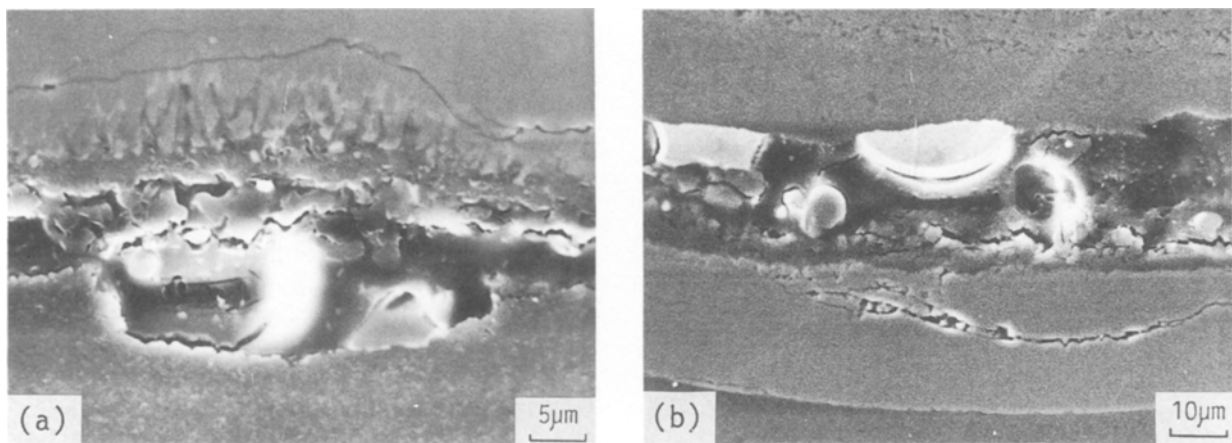


Figure 2 Secondary electron images of coating layers of sample P-31 particle. (a) Corrosion of the SiC layer, (b) opposite side to the corrosion.

is deposited at, the corroded area of the SiC layer. No fission product was detected in the area except for a small amount of cerium, which may be oxide. Other rare-earth elements, such as neodymium and lanthanum, were not observed. The white spots at the corroded area of the SiC layer in Fig. 1b may be cerium oxide, as in the case in Fig. 4. The coating layers on the cold side of the same particle are shown

in Fig. 5, where the white products or (Si, Ce, Ba) oxide are accumulated at the interface of the buffer-IPyC layers.

From Figs 2–5, it is probable that Si was transferred from the CO-SiC reaction area to the cold side of the particle through the buffer layer or the gap between the SiC and IPyC layers.

Silicon was also found in the UO₂ kernels of Triso-

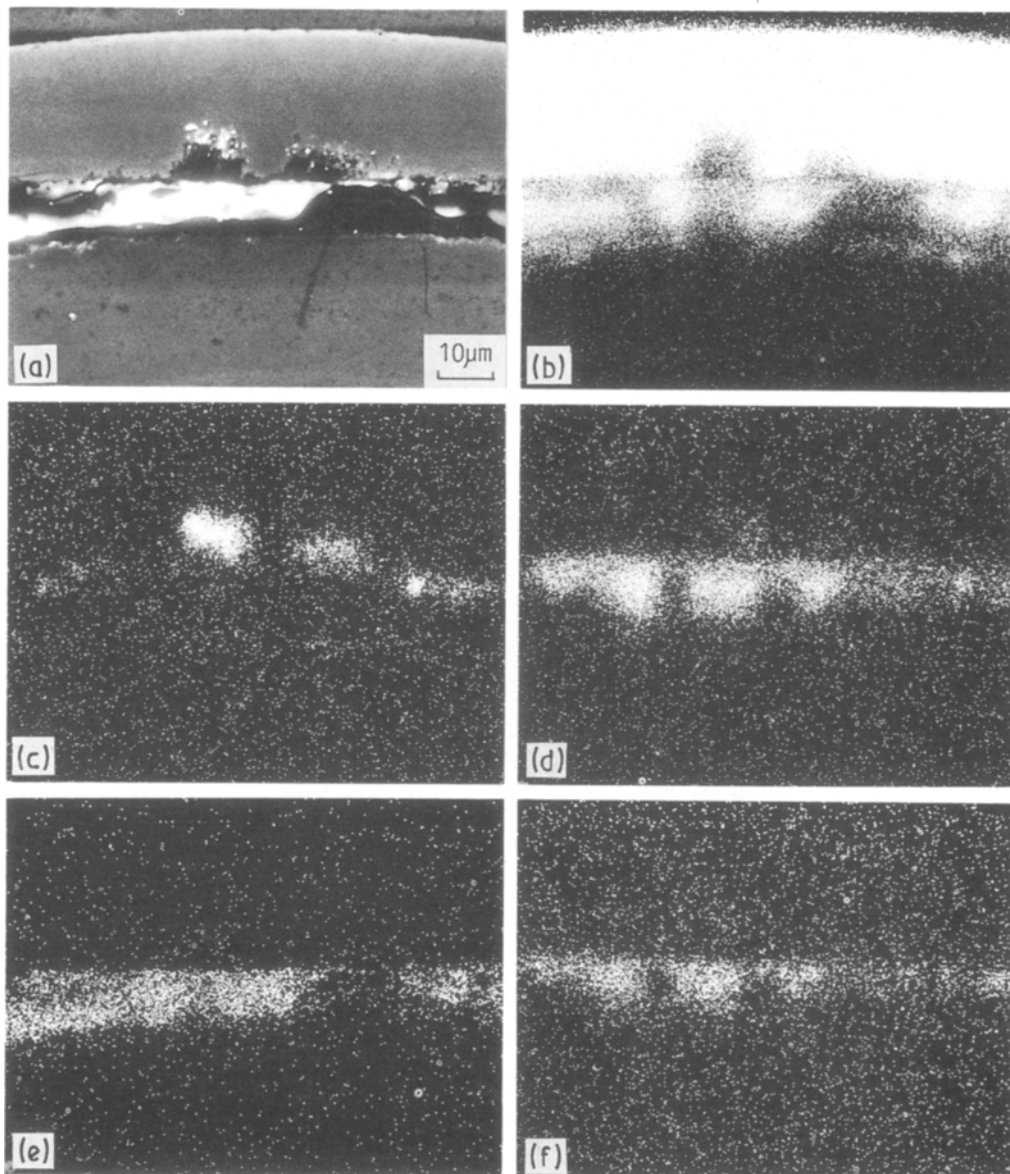


Figure 3 (a) Secondary electron image and X-ray images of (b) Si- K_{α} , (c) Pd- L_{α} , (d) Ba- L_{α} , (e) O- K_{α} and (f) Ce- L_{α} of coating layers on the cold side of sample P-52 particle.

coated particles with their SiC layers corroded. It is seen in Figs 6 and 7 that silicon reacted with palladium, rhodium, ruthenium, technetium and molybdenum to form silicides, although these elements form metallic inclusions in the intact Triso-coated UO_2 particles [14–16]. Two types of inclusion are seen in the sample P-61 particle shown in Fig. 6: (Pd, Rh, Ru, Tc, Mo) silicide and Pd–Rh–Ru–Tc–Mo alloy. The concentration of palladium is higher in the silicide than in the metallic alloy in the sample P-61 particle. On the other hand, three types of inclusion are seen in the sample P-31 particle shown in Fig. 7: molybdenum silicide, (Pd, Rh, Ru, Tc) silicide and (Pd, Rh, Ru, Tc, Mo) silicide. The thermodynamic stability of these silicides will be discussed in the next section.

The distribution of silicon (representative of the silicides) in the UO_2 kernel of sample P-22 is shown in Fig. 8. The silicides are distributed in the kernel without a sharp dependence on the temperature gradient.

4. Discussion

4.1. Thermodynamic analysis

4.1.1. In the coating-layers

In order to clarify the mechanism of the SiC corrosion by CO, thermodynamic analysis on the CO–SiC system was carried out. The computer code SOLGAS-MIX-PV [17] was used to calculate the equilibrium composition of the system. The calculation is based on the minimization of the total free energy of the system. Condensed and gaseous species considered in the calculation are listed in Table III. The necessary values for their standard enthalpy of formation at

TABLE III Species considered in the calculation

Condensed phase

β -SiC, SiO_2 (cristobalite, high), C(graphite), Si

Gas phase

CO, CO_2 , C, O_2 , SiO, SiO_2 , Si, Si_2 , Si_3 , SiC_2 , SiC, Si_2C

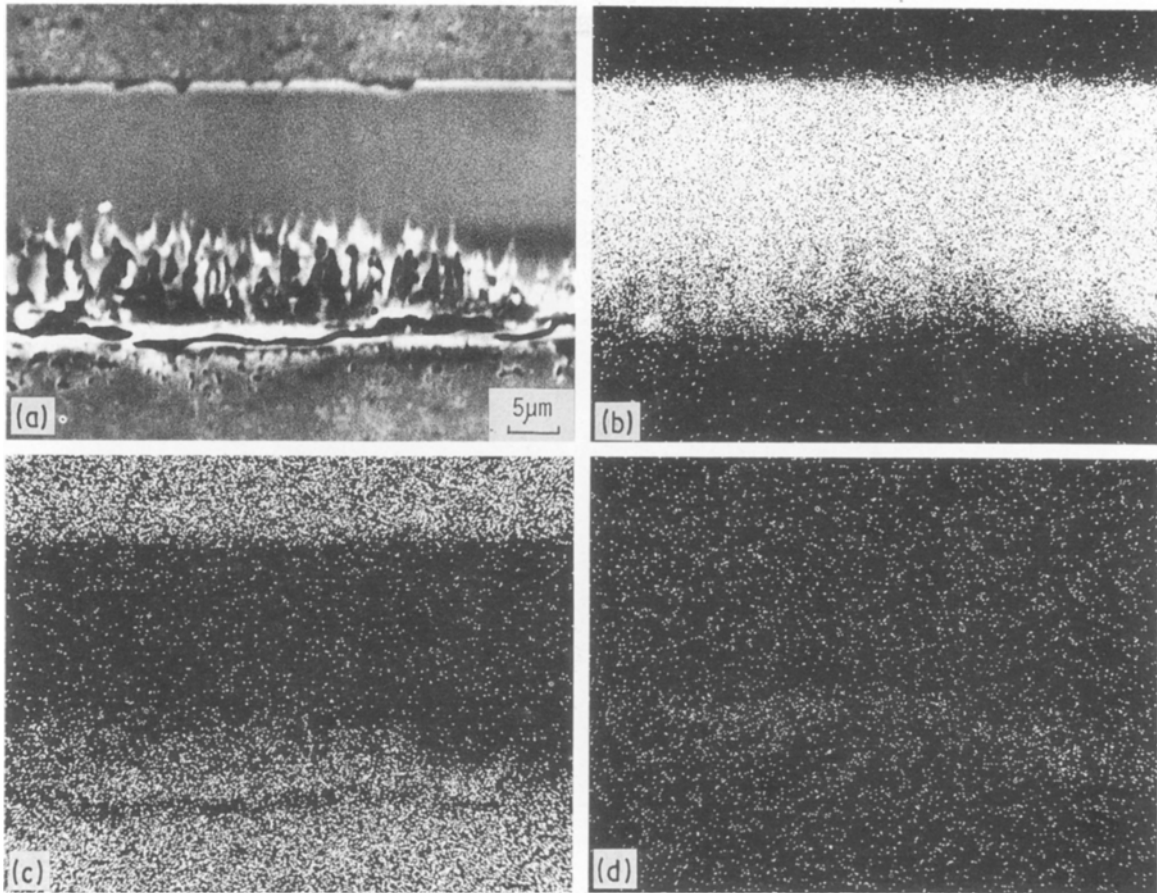


Figure 4 (a) Secondary electron image and (b) Si-K_α (c) C-K_α and (d) Ce-L_α X-ray images of coating layers on the hot side of sample P-22 particle.

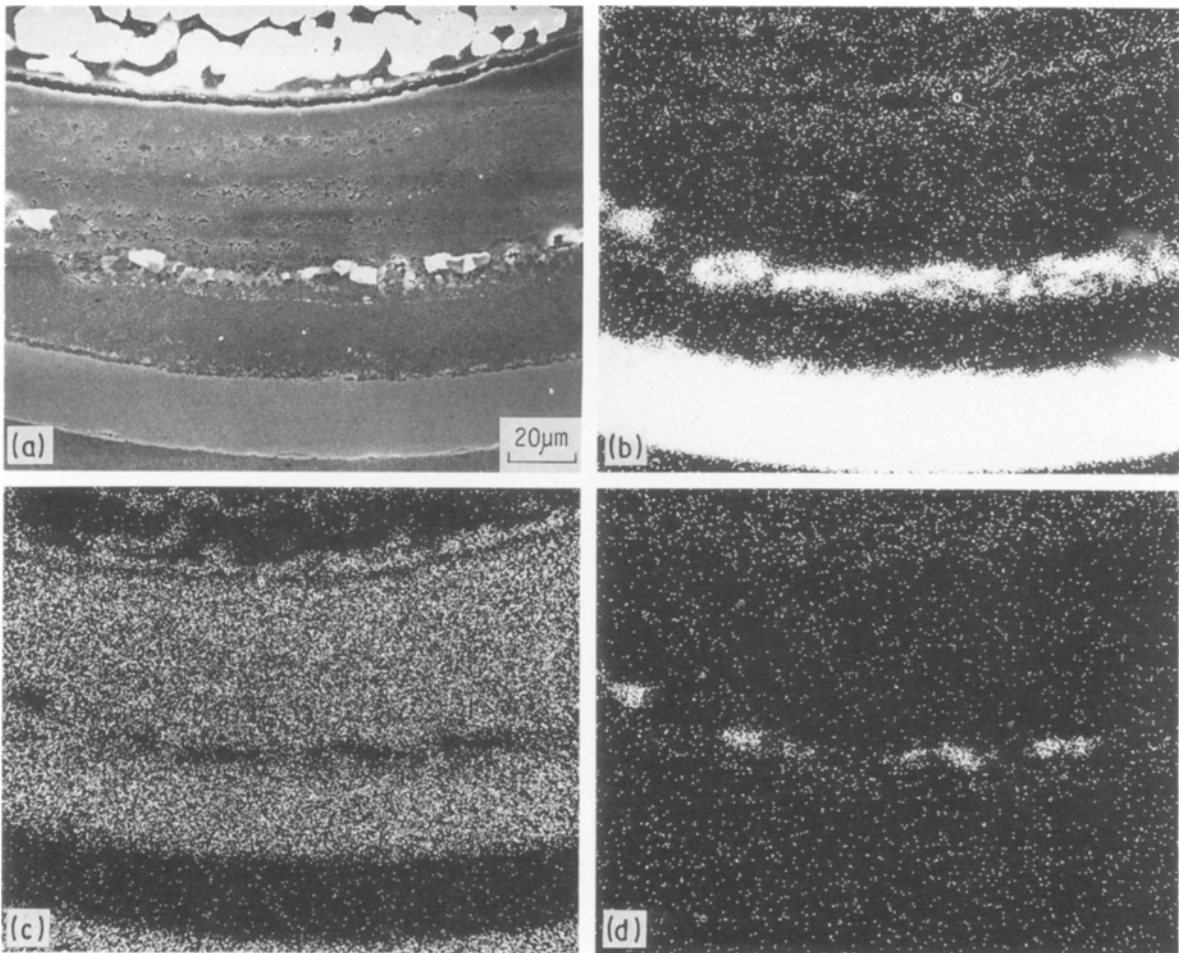


Figure 5 (a) Secondary electron image and (b) Si-K_α, (c) C-K_α and (d) Ce-L_α X-ray images of coating layers on the cold side of sample P-22 particle.

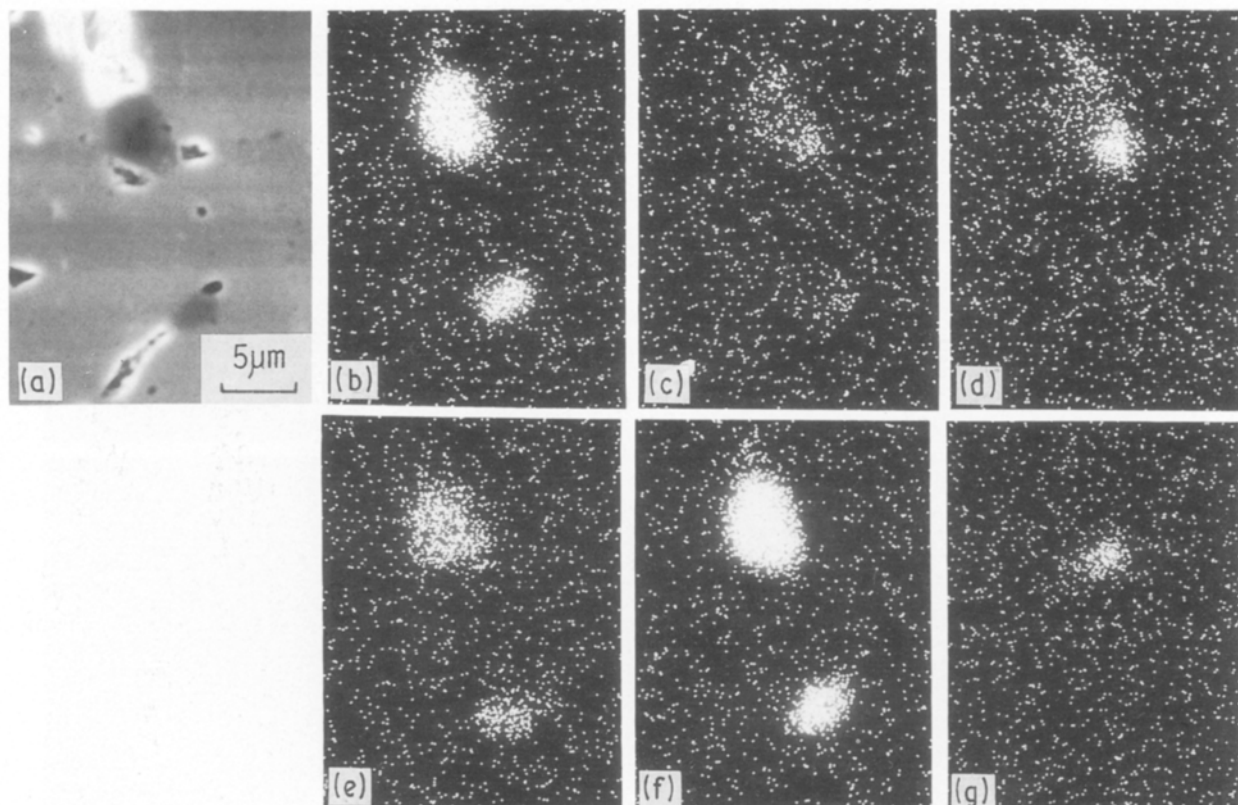


Figure 6 (a) Secondary electron image and X-ray images of (b) Ru- L_{α} , (c) Rh- L_{α} , (d) Pd- L_{α} , (e) Tc- L_{α} , (f) Mo- L_{α} and (g) Si- K_{α} in the kernel of sample P-61 particle.

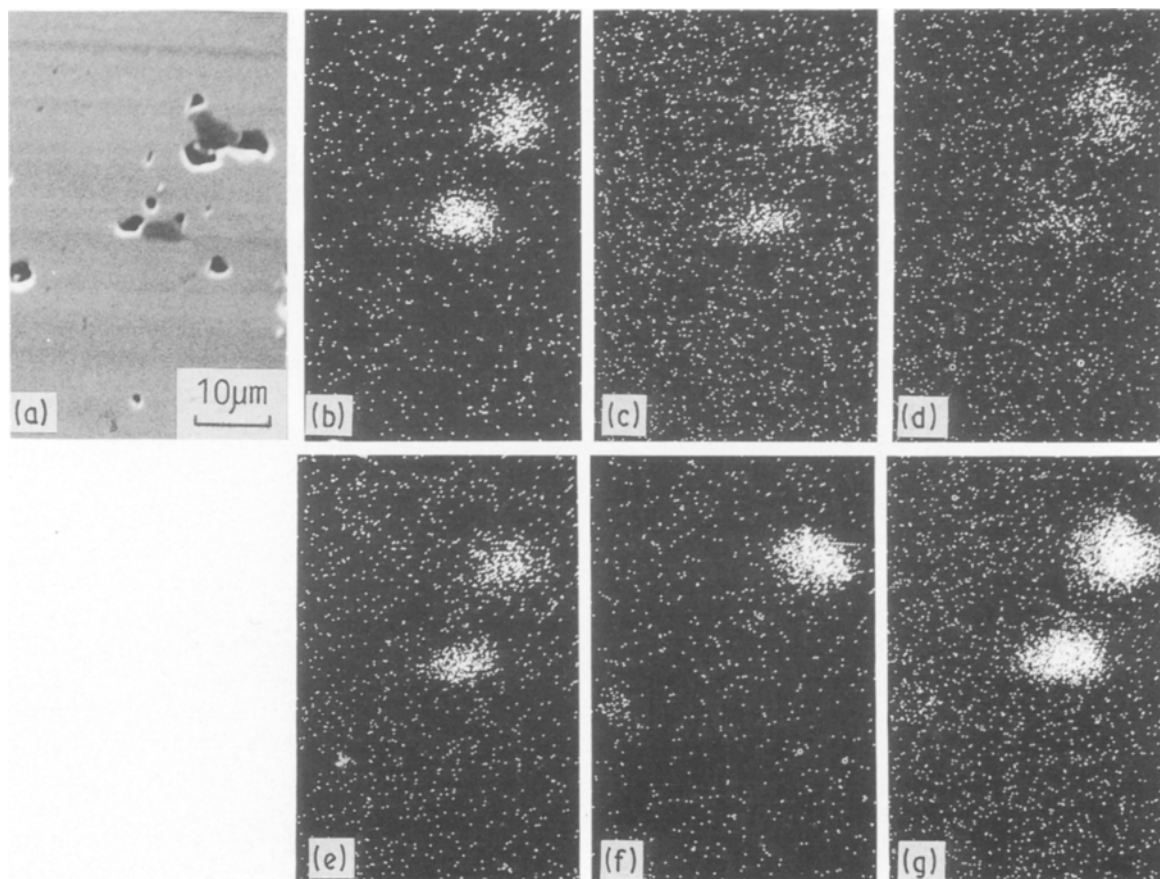


Figure 7 (a) Secondary electron image and X-ray images of (b) Ru- L_{α} , (c) Rh- L_{α} , (d) Pd- L_{α} , (e) Tc- L_{α} , (f) Mo- L_{α} and (g) Si- K_{α} in the kernel of sample P-31 particle.

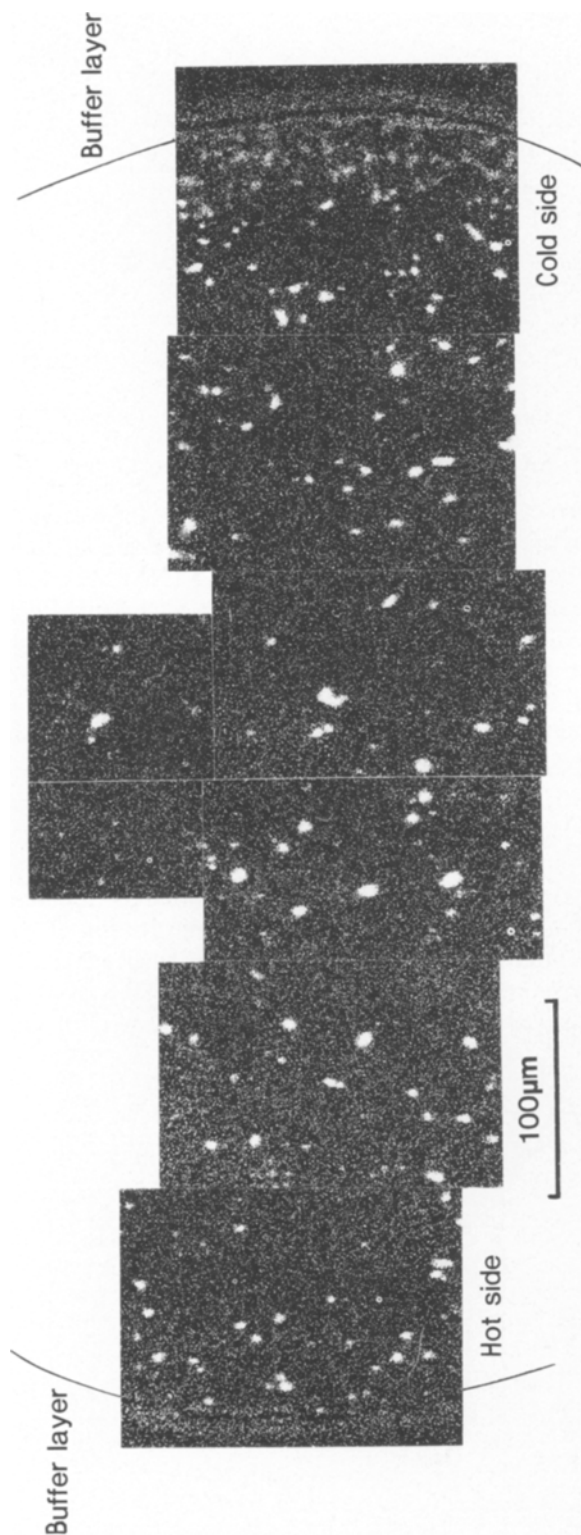


Figure 8 Si-K α X-ray image (representative of (Pd, Rh, Ru, Tc, Mo) silicide) in the kernel of sample P-22 particle.

298.15 K, $\Delta H_{f,298}^0$, and the free energy function, $(G^0 - H_{298}^0)/T$, were obtained from JANAF Thermochemical Tables [18].

The calculated equilibrium phase diagram of the CO–SiC reaction is shown in Fig. 9 with equilibrium CO pressure and temperature. According to the phase diagram, two different sets of products would be stable under the thermodynamic equilibrium: SiC(s) + C(s) (region 1) and SiO₂(s) + C(s) (region 2). Equilibrium vapour pressure of the gaseous species at 1500 and 1900 K are shown in Figs 10 and 11, respectively. These figures indicate that the main gaseous species is SiO(g) in the system and the vapour pressure of SiO(g) reaches its maximum at the boundary between the regions 1 and 2. The maximum SiO(g) pressures are 4.3×10^{-6} and 2.3×10^{-3} MPa at 1500 and 1900 K, respectively.

From the results of the calculation, the main equations of the chemical reaction could be deduced for each region of the diagram. In region 1 the chemical reaction



would occur under thermodynamic equilibrium. In region 2, on the other hand, the chemical reaction

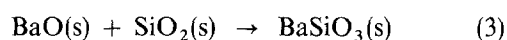


would occur, and the equilibrium vapour pressure of SiO(g) will still be as high as that in region 1.

The CO pressure generated in the irradiated Triso-coated UO₂ particle was calculated using the SOLGASMIX-PV [17] as a function of burn-up and temperature, considering the UO₂–FP–C system. Details of the calculation will be published elsewhere [19]. The calculated equilibrium CO pressure in the coated particles at 1500 and 1900 K is shown in Fig. 12 as a function of burn-up.

According to the conditions of CO pressure and the temperature of the irradiated coated particles, thermodynamic equilibrium would be achieved at the boundary between the regions in the irradiated Triso-coated particles with a failed IPyC layer: the chemical reaction expressed by Equation 2 would occur to reduce CO pressure to the value for the boundary between the regions. The high vapour pressure of SiO(g) suggests that silicon is transported as SiO(g) from the corroded area to the kernel or the cold side of the particle.

The presence of cerium and barium at the coating-layers was attributed to the high vapour pressure of CeO₂(g), BaO(g) and Ba(g) in the fuel [19]. Because the composition of (Si, Ce, Ba) oxide could not be determined in the present work, and available thermodynamic data for the oxides considered were limited, thermodynamic stability of BaSiO₃(s) was analysed. The chemical reaction expressed by



was considered and the Gibbs' free-energy changes in the reaction were calculated by the approximation [20]

$$\Delta G_T^0 = \Delta H_{f,298}^0 - T\Delta S_{298}^0 \quad (4)$$

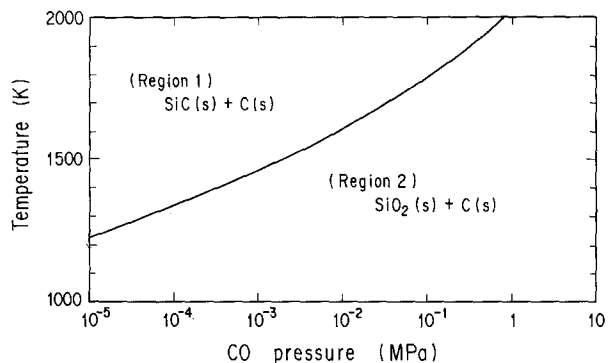


Figure 9 Calculated phase diagram of the CO-SiC reaction with equilibrium CO pressure and temperature.

where ΔG_T^0 is the difference between products and reactants of the standard Gibbs' free energy at T K, $\Delta H_{f,298}^0$ the difference in standard enthalpies of formation at 298.15 K, and ΔS_{298}^0 the difference in standard entropies at 298.15 K. The thermodynamic values for BaO(s) and BaSiO₃(s) were quoted from Kubaschewski and Alook [20] and SiO₂(s) from Stull and Prophet [18]. The free energy changes in Reaction 3 can be given by

$$\Delta G_T^0 = -159.1 + 0.009 T \text{ kJ mol}^{-1} \quad (5)$$

which indicates that BaSiO₃(s) would form thermodynamically at the temperatures of interest.

4.1.2. In the kernel

Thermodynamic stabilities of (Pd, Rh, Ru, Tc, Mo) silicides were estimated and compared to that of SiO₂(s). In the estimation Pd₂Si(s), Rh₂Si(s), Ru₂Si(s) and Mo₃Si(s) were considered, which are the most stable species in an oxidizing environment among Pd, Rh, Ru and Mo silicides whose thermodynamic data were available [20–22]. Four reactions were considered expressed by

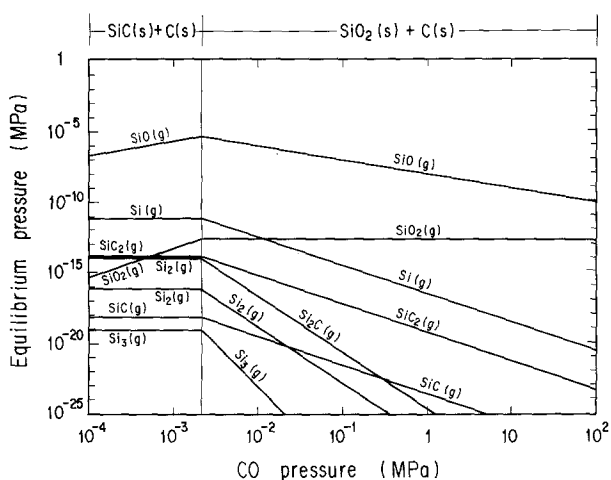
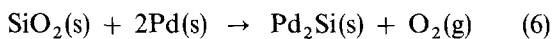


Figure 10 Equilibrium partial pressure of CO-SiC reaction at 1500 K.

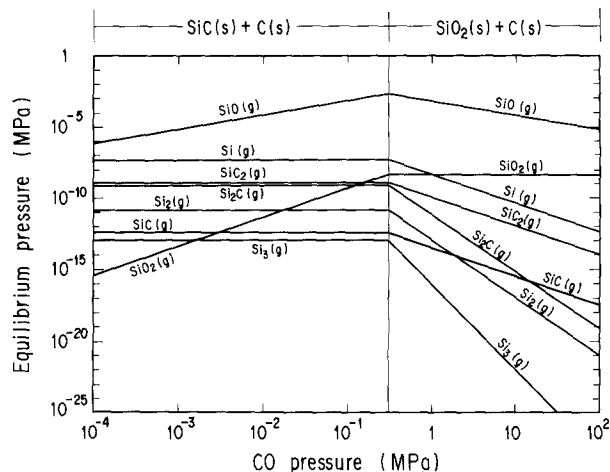


Figure 11 Equilibrium partial pressure of CO-SiC reaction at 1900 K.



To calculate the Gibbs' free energy of formation of the species with Equation 4, the thermodynamic values for SiO₂(s) were taken from JANAF Thermochemical Tables [18] and for Mo₃Si(s) from [20]. Because the thermodynamic data for noble metal (Pd, Rh and Ru) silicides have not been established [21–26], the enthalpies of formation of noble metal silicides used in the present work were the recent experimental value for Pd₂Si(s) [21] and the calculated values for Rh₂Si(s) and Ru₂Si(s) [22]. The values of ΔS_{298}^0 for noble metal silicides were neglected in the estimation, because the experimental value for ΔS_{298}^0 was not given and the estimated value for ΔS_{298}^0 of Pd₂Si(s) was small [23]. Substitution of the thermodynamic values into Equations 6–9 leads to the oxygen potentials of the reaction of SiO₂(s) with Pd(s), Rh(s), Ru(s) or Mo(s) to form each silicide,

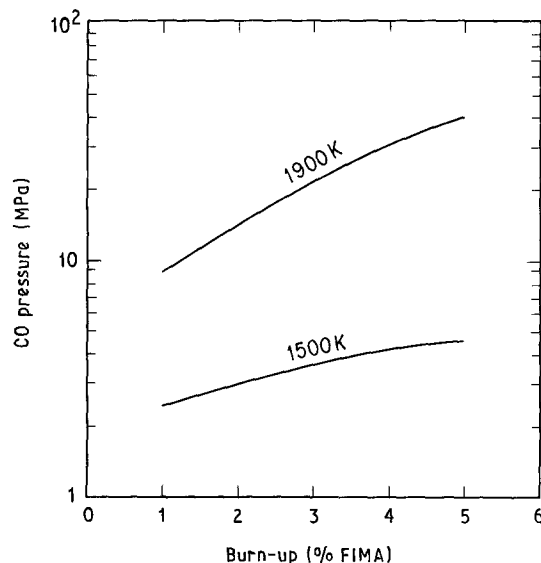


Figure 12 Calculated CO pressure in Triso-coated UO₂ particles as a function of burn-up at 1500 and 1900 K.

$\mu_{O_2}(\text{SiO}_2 \rightarrow \text{silicide})$, as a function of temperature

$$\begin{aligned} \mu_{O_2}(\text{SiO}_2 \rightarrow \text{Pd}_2\text{Si}) \\ = -712.0 + 0.1738 T \text{ kJ mol}^{-1} \end{aligned} \quad (10)$$

$$\begin{aligned} \mu_{O_2}(\text{SiO}_2 \rightarrow \text{Rh}_2\text{Si}) \\ = -792.5 + 0.1738 T \text{ kJ mol}^{-1} \end{aligned} \quad (11)$$

$$\begin{aligned} \mu_{O_2}(\text{SiO}_2 \rightarrow \text{Ru}_2\text{Si}) \\ = -792.5 + 0.1738 T \text{ kJ mol}^{-1} \end{aligned} \quad (12)$$

$$\begin{aligned} \mu_{O_2}(\text{SiO}_2 \rightarrow \text{Mo}_3\text{Si}) \\ = -789.2 + 0.1755 T \text{ kJ mol}^{-1} \end{aligned} \quad (13)$$

The oxygen potential at the boundary between regions 1 and 2 in Fig. 9, which is the thermodynamic equilibrium of CO–SiC reaction in the coated particles, is shown in Fig. 13 together with the oxygen potentials expressed by Equations 10–13. It is seen in Fig. 13 that molybdenum and noble metals would form silicides instead of a metallic alloy under thermodynamic equilibrium of the CO–SiC reaction in the coated particles. The observation that the metallic alloy is formed in the sample P-61 as shown in Fig. 6 indicates that thermodynamic equilibrium was not achieved in the coated particle. The observed tendency that silicon preferably reacted with palladium was consistent with the thermodynamic properties of molybdenum and noble metal silicides as shown in Fig. 13.

Although the oxygen potential of the observed coated particles in the present work was not measured, the oxygen potential in the coated particles with a corroded SiC layer could be estimated from Fig. 13. Because molybdenum silicide was observed in the kernels, the oxygen potential in the coated particles was estimated to be smaller than -500 kJ mol^{-1} at 1700 K. This value was smaller than the experimental values of between -500 and -375 kJ mol^{-1} , which

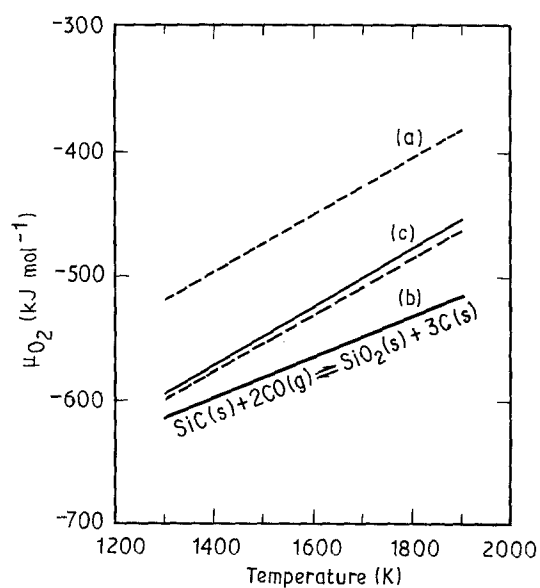


Figure 13 Oxygen potential at SiC(s)–C(s)–SiO₂(s) equilibrium and the oxygen potentials of reaction of SiO₂(s) with Pd, Rh, Ru or Mo to form silicide. (a) Oxygen potential expressed by Equation 10, (b) oxygen potential expressed by Equations 11 and 12, (c) oxygen potential expressed by Equation 13.

were calculated from the measurements of CO released from UO₂ in the intact coated particles [13]. This indicates that the oxygen potential was reduced by the CO–SiC reaction in accordance with the thermodynamic analysis. Mechanisms of the reduction of oxygen potential in the corroded SiC particles were just the same as those in the UO₂ kernel gettered with SiC [27].

4.2. Mechanism of SiC corrosion by CO

The mechanism of corrosion of the SiC layer by CO was presented based on the results of observations and thermodynamic analysis. A schematic representation of the mechanism of SiC corrosion by CO is shown in Fig. 14. Flowers and Horsley [3], and Stansfield [2] proposed mechanisms based on the thermodynamic analysis of the SiC–C–SiO₂ system, but the formation of (Pd, Rh, Ru, Tc, Mo) silicides was not considered in these mechanisms.

It is essential to the corrosion that the IPyC layer loses its function of protecting the SiC layer from CO. Usually, the corrosion is caused by the failure of the IPyC layer which results from the irradiation-induced shrinkage of the IPyC layer [28]. The irradiation performance of the PyC layer is dependent on its quality as well as irradiation conditions [29]. A gas-permeable IPyC layer [30], which can in no way be acceptable as the IPyC layer, will result in SiC corrosion by CO. Thus the quality control of the IPyC layer is important.

When CO comes into contact with the SiC layer, the SiC is oxidized to form SiO₂(s) and C(s) with a high vapour pressure of SiO(g). The growth of SiO₂(s) as a reaction product is restricted because the rate of vapour transport of SiO(g) from the corroded area to the cold side of the particle and the kernel is fast. Transported SiO(g) at the cold side of the particle reacts to form SiO₂(s) or more stable (Si, Ce, Ba) oxide if CeO₂(s) or BaO(s) is transported from the kernel. In the kernel SiO(g) reacts with metallic inclusions to form stable (Pd, Rh, Ru, Tc, Mo) silicides. As a result of these reactions, SiO₂(s) is not seen at the corroded SiC layer and CO is able to react with the SiC directly.

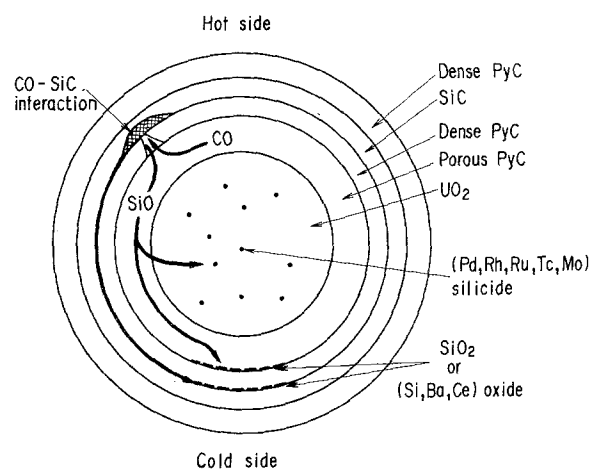


Figure 14 Schematic representation of the mechanism of corrosion of the SiC layer by CO in Triso-coated oxide fuel particles.

Formation of SiO₂(s) or (Si, Ce, Ba) oxide results in the reduction of CO pressure (oxygen potential) in the coated fuel particle.

5. Conclusions

The corrosion of the SiC layer by CO was observed in irradiated Triso-coated UO₂ particles by optical microscopy and electron probe micro-analysis. To understand the mechanism of the corrosion, thermodynamic analysis was carried out. From the observations and analysis, the following conclusions were drawn.

1. Mechanical failure of the IPyC layer was often observed beside the area of SiC corrosion. The grain boundaries of the SiC seemed to be selectively corroded during early stages of the corrosion.

2. Silicon dioxide or more stable (Si, Ce, Ba) oxide was accumulated at the buffer-IPyC or IPyC-SiC interfaces on the cold side of the particle. In the kernel, (Pd, Rh, Ru, Tc, Mo) silicides were observed. These resulted from the vapour transport of silicon monoxide from the corroded areas.

3. The mechanism of corrosion of the SiC layer by CO was determined, based on the observations and thermodynamic analysis.

4. The quality control of the IPyC layer is important to prevent the corrosion of the SiC layer by CO.

Acknowledgements

The authors thank Dr T. Kondo, Director of Department of Fuels and Materials Research, for his encouragement, and colleagues in the Hot Laboratory, Department of Research Reactor Operation, and in the Department of JMTR Project, for their co-operation.

References

1. E. PROKSCH, A. STRIGL and H. NABIELEK, *J. Nucl. Mater.* **136** (1985) 129.
2. O. M. STANSFIELD, "SiC Corrosion in TRISO I Coated (Th, U)O₂ Particles", Gulf General Atomic Report, Gulf General Atomic Company, Gulf-GA-B 12238 (September 1972).
3. R. H. FLOWERS and G. W. HORSLEY, "The Influence of Oxide Kernels on the Manufacture and Performance of Coated Particle Fuel", UKAEA Report, UK Atomic Energy Research Establishment, AERE-R 5949 (November 1968).
4. F. HOMAN, H. NABIELEK and L. YANG, "Low-Enriched Fuel Particle Performance Review", General Atomic Report, General Atomic Company, GA-A 14759 (August 1978).
5. W. BREMEN, A. NAOUMIDIS and H. NICKEL, *J. Nucl. Mater.* **71** (1977) 56.
6. G. ERVIN Jr, *J. Amer. Ceram. Soc.* **41** (1958) 347.
7. K. FUKUDA, T. OGAWA, S. KASHIMURA, K. HAYASHI, T. TOBITA, F. KOBAYASHI, K. MINATO, H. KIKUCHI, H. MURAKAMI, T. KIKUCHI, K. IKAWA and K. IWAMOTO, "Research and Development of HTGR Fuels", JAERI Report, Japan Atomic Energy Research Institute, JAERI-M 89-007 (February 1989).
8. K. MINATO, T. OGAWA, K. FUKUDA, K. IKAWA and K. IWAMOTO, "Electron Probe Micro-Analysis of Irradiated Triso-Coated UO₂ Particles (II)", JAERI Report, Japan Atomic Energy Research Institute, JAERI-M 84-002 (February 1984).
9. T. N. TIEGS, *Nucl. Technol.* **57** (1982) 389.
10. R. J. LAUF, T. B. LINDEMER and R. L. PEARSON, *J. Nucl. Mater.* **120** (1984) 6.
11. C. L. SMITH, *J. Amer. Ceram. Soc.* **62** (1979) 600.
12. F. J. HOMAN, T. B. LINDEMER, E. L. LONG Jr, T. N. TIEGS and R. L. BEATTY, *Nucl. Technol.* **35** (1977) 428.
13. T. B. LINDEMER and H. J. de NORDWALL, "An Analysis of Chemical Failure of Coated UO₂ and Other Oxide Fuels in the High-Temperature Gas-Cooled Reactor", Oak Ridge Report, Oak Ridge National Laboratory, ORNL-4926 (January 1974).
14. T. OGAWA, K. MINATO, K. FUKUDA and K. IKAWA, "Electron Probe Micro-Analysis of Irradiated Triso-Coated UO₂ Particles (I)", JAERI Report, Japan Atomic Energy Research Institute, JAERI-M 83-200 (November 1983).
15. H. KLEYKAMP, *J. Nucl. Mater.* **131** (1985) 221.
16. R. FÖRTHMANN, H. GRÜBMEIER, H. KLEYKAMP and A. NAOUMIDIS, in "Proceedings of The Thermodynamics of Nuclear Materials", edited by E. R. Beck (IAEA, Vienna, 1974) p. 147.
17. T. M. BESMANN, "SOLGASMIX-PV, A Computer Program to Calculate Equilibrium Relationships in Complex Chemical Systems", Oak Ridge Report, Oak Ridge National Laboratory, ORNL/TM-5775 (April 1977).
18. D. R. STULL and H. PROPHET, "JANAF Thermochemical Tables", 2nd Edn, NSRDS-NBS 37 (National Bureau of Standard, 1971).
19. K. MINATO, T. OGAWA, S. KASHIMURA, K. FUKUDA, M. SHIMIZU and Y. TAYAMA, submitted to *J. Nucl. Mater.*
20. O. KUBASCHEWSKI and C. B. ALOOK, "Metallurgical Thermochemistry", 5th Edn (Pergamon Press, New York, 1979).
21. L. TOPOR and O. J. KLEPPA, *Z. Metallkde.* **77** (1986) 65.
22. A. PASTUREL, P. HICTER and F. CYROT-LACKMANN, *Physica* **124B** (1984) 247.
23. T. OGAWA, "Thermodynamic Properties of Pd-Si System and Pd Attack on SiC Coating Layer", JAERI Report, Japan Atomic Energy Research Institute, JAERI-M 82-098 (August 1982).
24. R. CASTANET and R. CHASTEL, *Z. Metallkde.* **78** (1987) 97.
25. R. CASTANET, R. CHASTEL and C. BERGMAN, *J. Chem. Thermodyn.* **15** (1983) 773.
26. I. ARPSHOFEN, M. J. POOL, U. GERLING, F. SOMMER, E. SCHULTHEISS and B. PREDEL, *Z. Metallkde.* **72** (1981) 776.
27. G. W. HORSLEY, G. J. WELDRICK, J. A. TURNBULL and R. SHIPP, *J. Amer. Ceram. Soc.* **59** (1976) 1.
28. L. J. KAAE, *Nucl. Technol.* **35** (1977) 359.
29. D. P. HARMON and C. B. SCOTT, *ibid.* **35** (1977) 343.
30. D. P. STINTON, B. A. THIELE, W. J. LACKEY and C. S. MORGAN, *Amer. Ceram. Soc. Bull.* **61** (1982) 245.

Received 9 October 1989
and accepted 24 April 1990